1 **Using kinetic energy measurements from altimetry to detect shifts in the**

2 **positions of fronts in the Southern Ocean**

3 Don P. Chambers[1]

4 [1] College of Marine Science, University of South Florida, St. Petersburg, FL

5 Correspondence to: D. Chambers (donc@usf.edu)

6

7 **Abstract.** A novel analysis is performed utilizing cross-track kinetic energy (CKE) computed

8 from along-track sea surface height anomalies. The mid-point of enhanced kinetic energy

9 averaged over three-year periods from 1993 to 2016 is determined across the Southern Ocean

10 and examined to detect shifts in frontal positions, based on previous observations that kinetic

11 energy is high around fonts in the Antarctic Circumpolar Current system due to jet instabilities. It

12 is demonstrated that although the CKE does not represent the full eddy kinetic energy (computed

13 from crossovers), the shape of the enhanced regions along groundtracks is the same, and CKE

14 has a much finer spatial sampling of 6.9 km. Results indicate no significant shift in the front

15 positions across the Southern Ocean, on average, although there are some localized, large

16 movements. This is consistent with other studies utilizing sea surface temperature gradients, the

17 latitude of mean transport, and probability of jet occurrence, but is inconsistent with studies

18 utilizing the movement of contours of dynamic topography.

1. INTRODUCTION

There is as much we don't know about the circulation of the Southern Ocean as we do. Although the current system is routinely called the Antarctic Circumpolar Current (ACC), it consists of several fronts with distinct water properties to the north and south of the fronts (Nowlin and Clifford, 1982; Orsi et al., 1995; Belkin and Gordon, 1996). The most significant of these fronts, responsible for the majority of the ACC volume transport (e.g., Cunningham et al., 2003), are the Subantarctic Front (SAF) and the Polar Front (PF). However, even this is not a realistic picture of the circulation in the Southern Ocean, since at any specific time, there can be from three to ten narrow jets around the fronts that are highly variable in strength and location, masking the specific frontal boundary (Sokolov and Rintoul, 2007, 2009a, 2009b; Sallee et al., 2008; Thompson et al., 2010; Thompson and Richards, 2011; Langlais et al., 2011; Graham et al., 2012; Chapman, 2014; Gille, 2014; Kim and Orsi, 2014; Shao et al., 2015; Chapman, 2017a). Although positions of fronts have been estimated throughout the Southern Ocean, primarily using gradients of subsurface density measured from hydrographic sections (Orsi et al., 1995), contours of dynamic topography (Sokolov and Rintoul 2007, 2009a, 2009b; Langlais et al., 2011), or a combination Kim and Orsi (2014), in many places there are no strong currents that can be measured near the front position (Chapman, 2014; 2017a).

Because of the highly variable nature of jets and the lack of clear observational detection of fronts in some areas, the literature has become muddled over the difference between a front and a jet, primarily because the "front" is rarely observed at any specific time due to the high-variability of jets (Thompson et al., 2010; Thompson and Richards, 2011; Chapman 2014; 2017a). However, even in the presence of highly variable jets, methods have been developed to determine mean fronts positions in a probabilistic sense. Thompson et al. (2010) demonstrated

42 one could define fronts in the Southern Ocean by computing probability density functions of

43 potential vorticity in an eddy-resolving general ocean circulation model. Chapman (2014, 2017a)

44 later showed this could also be done using localized gradients in dynamic topography (i.e., high

45 geostrophic velocity) using satellite altimeter observations, but again, only as statistical

46 probability. This is because these areas of enhanced gradients and velocity are more reflective of

47 jets, which strengthen and die, appear and disappear, bifurcate and join back together. Because of

48 this, they can only be detected on average 10-15% of the time. However, Chapman (2014,

49 2017a) has demonstrated that, at least in a mean sense, fronts defined by mean dynamic

50 topography contours (commonly known as the "contour method") do lie within the probability

51 distribution inferred from "gradient" methods.

52   An open question is how the fronts and jets that comprise the ACC will respond in a

53 warming climate. Analysis of climate models (which cannot simulate jets in the Southern Ocean)

54 suggests that as the atmosphere warms, the winds that drive the fronts and jets of the ACC will

55 migrate south (e.g., Fyfe and Saenko, 2006; Swart and Fyfe, 2012). It should be noted, however,

56 that the mean position of the southern hemisphere westerlies in the models lies significantly

57 equatorward of the true position (e.g., Figure 2 in Fyfe and Saenko, 2006). Thus, it is not entirely

58 clear whether the model is predicting a true shift in the wind position, or whether the model has

59 not yet reached equilibrium with winds in the proper location.

60   Still, based on these model results, researchers have been testing the hypothesis that as winds

61 in the Southern Ocean shift south, the frontal positions and jets will also migrate south. So far,

62 the results are mixed. Using the contour method and tracking how the dynamic topography

63 contours associated with a front position shift in time, Sokolov and Rintoul (2009b) found that

64 the SAF and PF had both moved south by approximately 60 km over 15 years between 1993 and

65 2008. Kim and Orsi (2014) recently updated this analysis and found that while the average

66 frontal position across the Southern Ocean indicates a strong southward shift, this is due

67 primarily to substantial shifts only in the Indian Ocean sector. They found no significant shifts

68 throughout the Pacific or Atlantic Ocean sectors using the contour method.

69   The primary assumption of these analyses is that if a contour of dynamic topography shifts

70 south, it is uniquely caused by a front moving south. This is not necessarily true. Gille (2014)

71 recently demonstrated that all contours in the Southern Ocean have shifted south on average, and

72 that this follows from the observed rise in sea level – as the sea surface height rises, the contours

73 will appear to shift south. While this breaks down at the far south and north of the ACC where

74 dynamic topography gradients are small, these areas are far away from the PF and SAF and so

75 have not been considered in previous analyses. Gille (2014) used a different measure to

76 determine the position of the ACC fronts, based on the latitude of the mean surface transport of

77 the ACC measured by altimetry, which is in essence a mean location of all the jets in the

78 Southern Ocean. She found no significant shift on average, but considerable interannual

79 variability, especially regionally.

80   Another factor other than sea level rise can cause the dynamic topography contour to shift

81 south -- if the magnitude and width of the jet has changed. This is demonstrated in **Figure 1**,

82 where we show the mean dynamic topography from two jet scenarios: 1) where the peak of two

83 Gaussian shaped jets have shifted south, and 2) where the peak has not shifted, but the magnitude

84 has decreased, the width has broadened, and the shape has become slightly skewed. Although the

85 resulting topography profiles are not identical, they are similar, and both suggest a southward

86 movement of dynamic topography contours.

87   Researchers using other methods also find little or no southern migration of the fronts or jets

88   in the Southern Ocean as a whole. Graham et al. (2012) used a high-resolution model to show

89   that the Polar Front and Subantarctic Front are constrained by bathymetry, even in increasing and

90   shifting winds. Shao et al. (2015) utilized the skewness of sea level anomalies to identify front

91   positions, and found no southward motion, but did find changes in the east Pacific correlated

92   with the Southern Annual Mode. Chapman (2017a), using positions of fronts determined from

93   the probability of jet locations, also found no significant southward movement, but high

94   interannual variability. Finally, Freeman and Lovenduski (2016a) used weekly estimates of the

95   Polar Front position determined from satellite sea surface temperature (SST) gradients to show

96   no significant southward shift between 2002 and 2014 on average, except in the Indian Ocean.

97   They also found a statistically significant northward shift of the PF in part of the south Pacific.

98   Thus, recent studies all agree that the Subantarctic Front and Polar Front have not shifted

99   south, even though there is evidence the winds have shifted south in the austral summer months

100   (Swart and Fyfe, 2012). It should be noted that when averaged over the full calendar year,

101   however, there has been no significant shift in the wind position (Swart and Fyfe, 2012).

102   In this paper, we develop a new method to study variability in the position of the fronts in the

103   Southern Ocean, based on tracking the location of envelopes of kinetic energy measured by

104   satellite altimetry. It is known from modeling studies that the front positions are associated with

105   increased kinetic energy, due to instabilities in the jets and interactions with bathymetry

106   (Thompson et al., 2010; Thompson and Richards, 2011). After demonstrating that kinetic energy

107   computed from along-track satellite altimetry forms relatively wide envelopes of enhanced

108   energy that occur within the probability range of jets and fronts (e.g., Chapman, 2017a), we track

109   the positions of these envelopes from 1993 until 2016 to quantify if the envelopes have shifted

110   south by a statistically significant amount. This is based on the assumption that if the front and

111   jets around the front have shifted south, then the envelope of high kinetic energy should also

112   move by a comparable amount. Since the kinetic energy calculation is based on estimating

113   gradients of sea level anomalies, this approach is similar to other gradient methods for detecting

114   fronts or jets (e.g., Chapman, 2014; 2017a; Gille, 2014; Freeman and Lovenduski, 2016a). It

115   differs from these approaches, however, in that instead of determining individual gradients and

116   tracking these over time, it looks for regions of high gradients (i.e., high energy) surround by

117   regions of low gradient (i.e., low energy). This allows us to detect envelopes for every time-

118   period considered, instead of only a fraction of the time, allowing for better tracking of the

119   change over time.

120   Section 2 will describe the data and methods used, while section 3 will present results,

121   including evaluation of the method for detecting mean positions of fronts and for tracking their

122   change over time. Section 4 will discuss the results in the context of previous studies and

123   evaluate the usefulness of the method.

124   **2. DATA AND METHODS**

125   We utilize geostrophic surface current anomalies computed from the 24-year record of 1-Hz

126   sea surface height (SSH) data along the TOPEX/Poseidon (T/P) groundtrack in the Southern

127   Ocean (**Figure 2**). The altimetry data used are from four separate altimeter missions:

128   TOPEX/Poseidon (January 1993 – January 2002), Jason-1 (February 2002 – July 2008), Jason-2

129   (August 2008 – August 2016), and Jason-3 (August 2016 – December 2016). Because the

130   official TOPEX/Poseidon (T/P) geophysical data records (GDRs) have not been updated since

131   the late 1990s, we utilize the corrected data products from the Integrated Multi-Mission Ocean

132   Altimeter Data for Climate Research provided by Beckley et al. (2010) at the NASA PO.DAAC

133   site (https://podaac.jpl.nasa.gov/Integrated_Multi-Mission_Ocean_AltimeterData). Jason-1 data

134   are from the GDR-C version and were downloaded from the NASA PO.DAAC site in June 2010.

135   Jason-2 are from the GDR-D version and were downloaded from NOAA NODC

136   (ftp://ftp.nodc.noaa.gov/pub/data.nodc/jason2) between August 2012 and June 2016. Jason-3 are

137   also from the GDR-D version and were downloaded from NOAA NODC

138   (ftp://ftp.nodc.noaa.gov/pub/data.nodc/jason3) on August 7 and 8, 2017.

139   We utilize the 1-Hz along-track SSH data from the four altimeters and compute sea level

140   anomalies by interpolating the DTU10 mean sea surface model (Andersen and Knudsen, 2009;

141   http://www.space.dtu.dk/english/Research/Scientific_data_and_models/downloaddata) to the

142   SSH location using bilinear interpolation. The DTU10 mean sea surface model is based on SSH

143   from multiple altimeters averaged over 17 years in a rigorous and consistent manner (Andersen

144   and Knudsen, 2009). T/P, Jason-1, and Jason-2 data were all included. All recommended

145   geophysical and surface corrections (e.g., water vapor, ionosphere, sea state bias, ocean tides,

146   inverted barometer, etc) have been applied, to correct for biases introduced by atmospheric

147   signal refraction and sea state effects (e.g., Chelton et al., 2001).

148   We utilize this record rather than the gridded products based on mapping SSH from multiple

149   altimeters (e.g., Ducet et al., 2000; Pujol et al., 2016), because the along-track data have a finer

150   resolution in space (6.9 km along the groundtrack) and we recently demonstrated that the

151   mapped altimetry data underestimated eddy kinetic energy (EKE) throughout the Southern

152   Ocean compared to using along-track data by as much as 60-70% (Hogg et al., 2015). While the

153   along-track sea level anomalies are filtered to reduce noise and thus may attenuate some signal,

154   the filtering used (described later in this section), is less than that used for the mapped data,

155   which uses observations from as long as 20 days and 200 km away to influence the mapped

156   value. By filtering only alongtrack data, the time differences are small (a few minutes at most),

157   and the spatial influence is less than 100 km. Tests with unfiltered data accounting for estimated

158   random noise in the sea level anomaly data suggests attenuation of kinetic energy is minimal

159   with this approach and, more importantly, that the shape of the kinetic energy envelope does not

160   significantly change.

161   One can only compute EKE from alongtrack data at crossover points, where the ascending

162   and descending groundtracks cross (Figure 2). Knowing the groundtrack angle with the north

163   meridian (θ) one can compute the zonal ($d\eta/dy$) and meridional gradients ($d\eta/dx$) of SSHA

164   directly from the gradients of SSHA for the ascending pass ($d\eta/dr_{asc}$) and descending pass

165   ($d\eta/dr_{des}$) using simple geometry (Parke et al., 1987)

166
$$\frac{d\eta}{dy} = \frac{\left[\dfrac{d\eta}{dr_{asc}} - \dfrac{d\eta}{dr_{des}}\right]}{2\sin\theta}, \frac{d\eta}{dx} = \frac{\left[\dfrac{d\eta}{dr_{asc}} + \dfrac{d\eta}{dr_{des}}\right]}{2\cos\theta}, \tag{1}$$

167   noting that this formulation assumes the gradients represent the derivative of the northern SSHA

168   relative to the southern SSHA (for both the ascending and descending passes). Once this is

169   computed, the velocities can be computed directly from the zonal and meridional gradients:

170
$$u = -\frac{g}{f}\frac{d\eta}{dy}, v = \frac{g}{f}\frac{d\eta}{dx}, \tag{2}$$

171   where g is the acceleration due to gravity, and f is the Coriolis parameter

172   This formulation assumes that the velocity field has not changed significantly between the

173   times the two passes fly over the crossover point. At high latitudes, the majority of crossovers (>

174   78%) have a time separation of less than 3 days. At 40°, the average propagation speed of an

175   eddy is about 3 cm s^{-1} [Chelton et al., 2007], meaning the eddy would have only been displaced

176   by 8 km at most over this period. At higher latitudes, this is even less. Considering the diameter

177   of eddies at these latitudes are of order 100 km [Chelton et al., 2007], the movement is not large

178   enough to cause a significant change in velocity at the point. The primary problem with

179   velocities computed from crossovers is the smaller number compared to using gridded data, or

180   the time-varying, anomalous geostrophic current normal to the groundtrack (u_T). This can be

181   computed directly from the derivative of the SSH anomaly (η) along the ground-track distance

182   (*dr*) from

183
$$u_T = -\frac{g}{f}\frac{d\eta}{dr}.$$
(3)

184   This cross-track current is a projection of both the zonal (*u*) and meridional (*v*) components of

185   the full anomalous velocity field. However, neither *u* nor *v* can be determined unambiguously

186   from $u_{T..}$ Here, we merely examine the variability of u_T without making any assumptions

187   concerning how it may be related to the full velocity, or *u* and *v*.

188   Because derivatives of SSHA (Equations 1 and 3) have to be computed numerically (here,

189   center-differences are used) and η contains significant noise at the 1 Hz sampling-rate of the

190   altimeters, we optimally interpolate η along-track using a model of the covariance of the signal

191   and error. We used the method of Wunsch (2006, Chapter 3) and a covariance function modeled

192   as a Gaussian with a roll-off of 98 km and random noise of 2 cm, which was determined from the

193   autocovariance of all TOPEX/Poseidon, Jason-1, and Jason-2 SSHA data from 1993-2015

194   between 40°S and 65°S.

195   Once $u_T(t)$ was computed at each 1-sec bin along the groundtracks in Figure 2 for each 10-

196   day repeat cycle, the cross-track kinetic energy (CKE) was computed as CKE(*x,t*) = 0.5 $u_T(x,t)^2$,

197   where *x* here is used to denote a generic 1-sec bin along the ground track. We also computed the

198   full EKE at the more limited crossover points as $EKE(x,t) = 0.5(u(x,t)^2 + v(x,t)^2)$.

199   The CKE values were averaged over the entire 24-year record and examined for each

200   groundtrack segment (both ascending and descending) to judge where CKE was exceptionally

201   high (Figure 3). We also computed CKE using the raw values of η with no optimal interpolation

202   and compared to that computed with optimal interpolation. The locations of high CKE were the

203   same, although values were significantly higher with the unsmoothed data. The quiescent regions

204   of the ocean also showed considerably more noise, making it more difficult to determine

205   boundaries of elevated CKE. For this reason, the values determined from the optimally

206   interpolated data were used.

207   Several criteria were utilized to quantify where the high CKE values were considered to be

208   associated with fronts. First, we constrained the southern boundary to be 5° south of the Orsi et

209   al. (1995) values of the PF and the northern boundary to be 5° north of the SAF. Secondly, we

210   used a lower-limit for CKE of 200 cm^2 s^{-2} for detection and tested that the width of the envelope

211   of high CKE above the lower-limit was at least 100 km. The requirement that the envelope be

212   greater than 100 km was done to reduce the impact of eddies in an otherwise quiescent region,

213   since the diameter of eddies in the Southern Ocean is about 100 km. The CKE lower-limit was

214   determined via iteration with different limits. For each case, the average center of the CKE

215   envelope averaged over 24-years (based on the mean of the first and last points to exceed the

216   lower-limit) was computed and compared visually to the Orsi et al. (1995) front positions. 200

217   cm^2 s^{-2} was selected because there were a significant amount of CKE envelope centers clustered

218   around the Orsi et al. (1995) fronts and the envelopes were found for every 10-day repeat cycle.

219   Using a higher limit resulted in fewer detections, especially when smaller time-averages were

220   used. Using a lower limit, we could find more potential front positions based on CKE, but many

221   were far from the front positions estimated by Orsi et al (1995).

222   An example of a detected high CKE envelope is shown in Figure 3, based on the average of

223   CKE between 1993 and 2015 computed from T/P-Jason satellite pass 207 in the south Indian

224   Ocean. This pass starts at 64.3°S near the prime meridian and extends to 41.2°S and 41°E

225   longitude. There is clearly a wide envelope of enhanced CKE greater than 200 cm^2 s^{-2} between

226   55°S and 47°S.

227   The mean CKE profile pictured in Figure 3 has multiple local maxima, most likely associated

228   with variability of the narrow jets that surround the front. As shown by Chapman (2017a), these

229   jets (evidenced in higher gradients of SSHA) do not occur around a front 100% of the time. At

230   most, they occur about 30% of the time, and more often less than 15% of the time. Figure 4

231   shows the behavior of CKE along this pass for different 3-year periods. Note that the number of

232   clearly defined maxima ranges from a low of 4 for the 2014-2016 average to 9 in 1993-1995.

233   While other studies have estimated positions of these maxima in SSHA gradients on daily

234   intervals (e.g., Chapman, 2017a), one does not obtain a consistent number of maxima each time,

235   making the determination of shifts difficult. Moreover, note that although there are two general

236   peaks in CKE in the long-term mean profile, the minimum between them is still higher than 200

237   cm^2 s^{-2}. A minimum is also not well defined in several of the shorter averaging periods (for

238   example, 2008-2010).

239   Thus, instead of attempting to track all the maxima of CKE individually – analogous to

240   tracking steepest gradients, as in Thompson et al. (2010), Graham et al. (2012), or Chapman

241   (2017a) – we track an estimate of the center of the envelope of enhanced CKE, as it exists in all

242   averaging periods. The assumption we make in doing this is that the localized maxima are

11

243   associated with variable jets, but the position of the envelope of high CKE is related to the front.

244   There are many different ways to compute a "center" of the envelope, ranging from the

245   average of the two end points, to a centroid calculation, to computing the point where the integral

246   of CKE over distance is balanced on both sides, which we call the "half-power point." We have

247   selected the latter to use, as it defines a "center" closer to the peak of CKE in the envelope. This

248   is advantageous when the CKE curve is slightly skewed, with less magnitude on one side and

249   more on the other. Assuming that the variability (and hence CKE) would be highest near the

250   front (i.e., what is assumed in studies using the gradient method), finding a center of the

251   envelope that is biased toward peak CKE is a reasonable approach.

252   The half-power point (x_{mid}) is computed so that

253 $$\int_{x_{south}}^{x_{mid}} CKE(x)\,dx = \frac{1}{2} \int_{x_{south}}^{x_{north}} CKE(x)\,dx \, , \tag{4}$$

254   where x_{south} and x_{north} are computed by first finding the maximum of CKE in the envelope above

255   200 cm^2 s^{-2}, then finding the first value to the north just below 25% of that peak along with the

256   similar value to the south (shown in Figure 3). Values other than 25% of the peak were tested.

257   Using value greater than this, up to 50%, resulted in no significant difference in the half-power

258   point. Using values smaller resulted in some boundaries not being defined. Thus, 25% of peak

259   CKE was considered reasonable. If multiple regions of enhanced CKE were found along the

260   same track, this process was carried out for each of them. This was done for all the 24-year mean

261   CKE profiles to establish the mean locations of the fronts between 1993 and 2016.

262   A similar procedure was done for CKE averaged over discrete 3-year intervals, starting in

263   January 1993 and ending in December 2016. A 3-year average was used to reduce the influence

264   of individual eddies on determining the envelope, and to reduce interannual variations in the

265   front position, which have been observed in other studies at some locations (e.g., Kim and Orsi,

266   2014; Shao et al., 2015). In particular, Kim and Orsi (2014) and Shao et al. (2015) found

267   significant correlation with the Southern Annular Mode, which has a quasi-biennial oscillation

268   (Hibbert et al., 2010). By averaging over three years, we found 8 distinct, statistically

269   uncorrelated samples of CKE for each groundtrack from which to deduce shifts in the half-power

270   point.

271   **3. RESULTS AND ANALYSIS**

272   The first thing tested was how well CKE represented the full EKE. If CKE does not have the

273   same general shape as EKE, then using it as a proxy for EKE to determine high energy envelopes

274   is not valid. After finding satellite passes with high CKE as discussed in Section 2, EKE was

275   computed along the same pass, using the crossover method (Equations 1 and 2).

276   Although CKE is lower than EKE along all groundtracks (see Figure 5 for examples), the

277   pattern of KE rise then fall is virtually identical. CKE, however, has the benefit of higher and

278   more regular sampling. Thus, we conclude CKE is a reasonable proxy for locating front positions

279   even though it may not be useful for quantifying the full energy of the anomalous currents.

280   Four general types of enhanced CKE were found (Figures 4 and 5). In most regions, the

281   envelope in CKE is more or less symmetrical (52% of cases). Only a few profiles have two

282   distinct regions of enhanced CKE that were identified, with a clearly defined minimum below

283   200 cm^2 s^{-2} between them in all time periods (3% of cases). 20% of the passes have multiple

284   peaks that vary in time but have no consistent minimum between the peaks (i e., Figure 4), while

285   25% have a skewed envelope (Figure 5), with a long rise in CKE followed by a sharp drop-off.

286   In all cases, though, the shape of the CKE envelope closely follows that of EKE, although the

287   amplitude was attenuated, by anywhere from 25-50%. Having closer samples of CKE, however,

288   allows for a better computation of the half-power point and possible shifts.

289   Figure 6 shows the locations of the half-power points determined from the mean CKE

290   profiles, along with estimate of the front position based on different methods: density gradients

291   from historical hydrographic sections (Orsi et al., 1995), dynamic topography contours (Kim and

292   Orsi, 2014), and the gradient of sea surface temperature (Freeman and Lovenduski, 2016a).

293   There are two estimates of the SAF and SACCF, and three of the PF. One of the PF estimates

294   (from Freeman and Lovenduski, 2016a) includes the standard deviation of the daily estimates.

295   It is important to note the large differences in estimates for the same front, which indicates

296   how uncertain these calculations are. For instance, in the Indian Ocean at 50°E, Freeman and

297   Lovenduski (2016a) find the PF at the same location that Orsi et al. (1995) found the SAF, while

298   Kim and Orsi (2014) find it significantly farther south. The SAF determination using the contour

299   method (Kim and Orsi, 2014) is substantially farther north than the one determined from

300   hydrographic data (Orsi et al., 1995) at most longitudes.

301   Many estimates from the half-power points of enhanced CKE occur between the same front

302   estimated by different methods, indicating they are at least within the uncertainty bounds of

303   frontal detection by other methods. Other values are at locations either north or south of the other

304   front estimates by as much as 3°, but it should be noted that the standard deviation of the PF

305   estimated by Freeman and Lovenduski (2016a,b) averages 2-3°, indicating these positions

306   estimated from CKE are well within the level of expected frontal variability.

307   Probably a better method for determining frontal position is to examine the probability of jets

308   occurring (Chapman, 2017a) (Figure 7). The CKE-defined mean front positions lie within the

309   probability envelopes, giving more confidence that the CKE measure is providing a comparable

310   measure of frontal position in many areas. The only location where CKE-defined fronts don't

311   agree well with the probability field from Chapman (2017a) is just west of the dateline, where

312   two points lie between levels of high jet (and hence front) probability.

313   Still, the good comparison is reassuring that the method developed in Section 2 is

314   successfully detecting regions of high energy related to jets around fronts. Since the movement

315   of jet positions has been used to estimate movement of the fronts (e.g., Chapman, 2017a), a

316   comparable calculation with positions of high CKE seems reasonable.

317   To quantify movement of the envelope of enhanced CKE, a linear trend is fit to the 8

318   estimations of the half-power point from 1993-2016 for each location shown in Figures 5 and 6.

319   Analysis of the residuals about the trend indicated they were random (lag-1 autocorrelation < 0.1

320   for all cases), so standard error was computed by scaling the formal error from the covariance

321   matrix determined in ordinary least squares by the standard deviation of the residuals. This was

322   also scaled up to account for the degrees of freedom lost by estimating the trend by sqrt(n/n_{EDOF}),

323   where $n = 8$, and $n_{EDOF} = 6$. Finally, the 90% confidence interval was computed by scaling by

324   1.94 for 6 effective degrees of freedom assuming a normal t-distribution of the residuals.

325   The results indicate considerable regional variability in the change of the half-power point

326   over 24 years, with large uncertainty bars (Figure 8). This is due to the substantial temporal

327   variability in the positions, which can be seen in Figure 4, where the leading edge of the CKE

328   envelope varies by over 1 degree of latitude (over 100 km) between 1993-1995 and 2011-2012.

329   To better see significant changes outside the uncertainty (90% confidence) interval, one can

330   compute the signal to noise ratio (SNR = trend/uncertainty). Examining this (Figure 9), one can

331   see there are some regions where the half-power point has moved southward by a significant

332   distance over the last 24 years (13.6% of points), but there are also points where it has moved

333   north (9.6%). For the majority of points (76.8%), there is no statistically significant change,

334   meaning no movement of the front is as likely as either a southward or northward shift due to the

335   high variability in 3-year positions.

336

337   **4. DISCUSSION AND CONCLUSIONS**

338   The results from the analysis of the positions of enhanced kinetic energy suggest no overall

339   shift in the frontal positions across the Southern Ocean, but some large, localized movements.

340   The region indicative of some southward shift between 90°E and 170°E is in approximately the

341   same area where Kim and Orsi (2014) and Freeman and Lovenduski (2016a) also reported large

342   shifts, between 1992 to 2011 and 2002 and 2014, respectively. However Freeman and

343   Lovenduski only examined the Polar front, and Kim and Orsi (2014) only found large shifts in

344   the PF and the southern ACC front. They found shifts of order 50-100 km in the SAF where the

345   points in this study cluster, which is considerably smaller than the individual shifts we find

346   between 90°E and 170°E along the SAF. However, the overall average over the region between

347   90°E and 170°E (-29 km per decade, or -66.7 km in 23 years), is consistent with what Kim and

348   Orsi (2014) found.

349   Kim and Orsi (2014) and Freeman and Lovenduski (2016a) also found slight northward

350   shifts in the front positions in the southeast Pacific, between 200°E-270°E. We also find some

351   locations in this region with a significant northward shift in the SAF. Kim and Orsi (2014) found

352   the shift of the SAF was about 30-40 km between 1992 and 2011. Our results suggest larger

353   shifts in some areas; averaged over the area, our results are 46 km per decade to the north, or 106

354   km from 1993-2015, which is consistent with the average over the region computed by Freeman

355   and Lovenduski (2016a) from sea surface temperature data, but for the Polar Front.

356   Kim and Orsi (2014) suggest that the shift of the fronts in the Indian Ocean were not directly

357   related to shifts in winds, but instead were caused by an expansion of the Indian subtropical gyre.

358   They linked the shift in the southeastern Pacific to wind changes related to mainly the Southern

359   Annular Mode in that region (Kim and Orsi, 2014).

360   Overall, this study supports the recent studies by Kim and Orsi (2014), Gille (2014), Freeman

361   and Lovenduski (2016a), and Chapman (2017a). All find that, while the frontal positions of the

362   ACC are highly variable in time, there is no statistically significant shift in the fronts to the south

363   on average. This study utilized a novel technique to reach this conclusion, which adds to the

364   robustness of evidence that there has not been a shift in the frontal positions. Thus, while the

365   fronts may eventually shift south in a warming climate, there is no strong evidence that it is

366   happening at the moment.

367   Other studies have shown significant positive trends in the Southern Ocean that have been

368   connected to the warming climate. These include changes in the ocean heat content in the upper

369   ocean between the 1930s-1950s and 1990s (e.g., Böning et al., 2008; Gille, 2008), increases in

370   the heat content of deep water between the 1990s and 2005 (e.g., Purkey and Johnson, 2010),

371   and increases in eddy kinetic energy in the Indian and Pacific Oceans since 1993 (Hogg et al.,

372   2015). Observational evidence of shifts in the winds, however, indicates that while there may be

373   a slight southward shift in winds during the southern hemisphere summer, the overall yearly

374   average shift is not significant (Swart and Fyfe, 2012). Thus, the growing consensus that fronts

375   have not shifted to the south, on average, is consistent with observations of no significant shift in

376   the yearly averaged winds.

377   The only evidence supporting a hypothesis that ACC fronts have shifted southward since the

378   1990s comes from mapping the location of contours of constant dynamic topography over time

379   (e.g., Sokolov and Rintoul, 2009b; Kim and Orsi, 2014). As Gille (2014) argued and as we have

380   demonstrated based on a simple thought experiment (Figure 1), there are other equally plausible

381   explanations for the apparent southern shift of the contours. Considering that four different

382   techniques – location of mean transport (Gille, 2014), maximum SST gradients (Freeman and

383   Lovenduski, 2016a), probability of jet positions (Chapman, 2017a), and the location of enhanced

384   kinetic energy (this study) – all agree that the fronts have not moved significantly on average,

385   one has to conclude that the method of using dynamic topography contours to detect changes in

386   front position is too sensitive to sea level rise be useful for determining shifts in frontal positions,

387   although it may prove useful for determining the mean position as Chapman (2017a) has argued.

388

389

Acknowledgements

REFERENCES

397 Andersen O B, and Knudsen P: DNSC08 mean sea surface and mean dynamic topography
398   models, *J. Geophys. Res.*, *114*, C11001, doi:10.1029/2008JC005179, 2009.
399 Beckley, B.D., Zelensky, N.P., Holmes, S.A., Lemoine, F.G., Ray, R.D., Mitchum, G.T., Desai,
400   S., and Brown, S. T.: Assessment of the Jason-2 Extension to the TOPEX/Poseidon, Jason-1
401   Sea-Surface Height Time Series for Global Mean Sea Level Monitoring, *Marine Geodesy,*
402   *33*(S1): 447-471, Supplemental Issue on OSTM/Jason-2 calibration/validation, Vol. 1, DOI:
403   10.1080/01490419.2010.491029, 2010
404 Belkin, I. M., and Gordon, A. L.: Southern Ocean fronts from the Greenwich meridian to
405   Tasmania, J. Geophys. Res., 101, 3675–3696, 1996.
406 Böning C. W., Dispert A., Visbeck M., Rintoul S. R., Schwarzkopf F. U.: The response of the
407   Antarctic circumpolar current to recent climate change. Nat Geosci., 1, 864–869, 2008.
408 Chapman, C. C.: Southern Ocean jets and how to find them: Improving and comparing common
409   jet detection methods, J. Geophys. Res. Oceans, 119, 4318–4339,
410   doi:10.1002/2014JC009810, 2014.
411 Chapman, C. C., New perspectives on frontal variability in the Southern Ocean, J. Phys. Ocean.,
412   47, 1151-1168, doi:/10.1175/JPO-D-16-0222.1, 2017a.
413 Chapman, C. C., Data from: New perspectives on frontal variability in the southern ocean. Dryad
414   Digital Repository. http://dx.doi.org/10.5061/dryad.q9k8r, 2017b.
415 Chelton, D. B., M. G. Schlax, R. M. Samelson, and R. A. de Szoeke: Global observations of
416   large oceanic eddies, Geophys. Res. Lett., 34, L15606, doi:10.1029/2007GL030812, 2007.
417 Cunningham, S. A., Alderson, S. G. , King, B. A., and Brandon, M. A.: Transport and variability
418   of the Antarctic Circumpolar Current in Drake Passage, J. Geophys. Res., 108(C5), 8084,
419   doi:10.1029/2001JC001147, 2003
420 Dong, S., Sprintall, J., and Gille, S. T. : Location of the Antarctic Polar Front from AMSR-E
421   Satellite Sea Surface Temperature measurements, J. Phys. Oceanogr., 36, 2075–2089,
422   doi:10.1175/JPO2973.1, 2006.
423 Ducet, N., Le Traon, P.-Y., Reverdin, G.: Global high resolution mapping of ocean circulation
424   from TOPEX/Poseidon and ERS-1 and -2. Journal of Geophysical Research 105 (C8),

425 19477–19498, 2000.

426 Fyfe, J. C., and Saenko, O. A.: Simulated changes in the extratropical Southern Hemisphere
427 winds and currents, Geophys. Res. Lett., 33, L06701, doi:10.1029/2005GL025332, 2006.

428 Freeman, N. M., Lovenduski, N. S.: Mapping the Antarctic polar front: weekly realizations from
429 2002 to 2014, Earth System Science Data, 8, 191-198, doi:10.5194/essd-8-191-2016, 2016a.

430 Freeman, N. M., Lovenduski, N. S.: Mapping the Antarctic polar front: weekly realizations from
431 2002 to 2014, links to NetCDF file and MPEG4 movie, PANGEA,
432 doi:10.5194/PANGEA.855640, 2016b.

433 Gille, S: Decadal-scale temperature trends in the Southern Hemisphere Ocean, J Climate, 21,
434 4749–4765, 2008

435 Gille, S. T.: Meridional displacement of the Antarctic Circumpolar Current, Philos. Trans. R.
436 Soc. A, 372, 20130273, doi:10.1098/rsta.2013.0273, 2014.

437 Graham, R. M., De Boer, A. M., Heywood, K. J., Chapman, M. R., and Stevens, D. P.: Southern
438 Ocean fronts: Controlled by wind or topography?, J. Geophys. Res. Oceans, 117, C08018,
439 doi:10.1029/2012JC007887, 2012.

440 Hibbert A, Leach H, Woodworth P, Hughes C, Roussenov V.: Quasi-biennial modulation of the
441 Southern Ocean coherent mode, Q. J. R. Meteorol. Soc., 136, 755 – 768.
442 DOI:10.1002/qj.581, 2010.

443 Hogg, A. McC., Meredith, M. P., Chambers, D. P., Abrahamsen, E. P., Hughes, C. W., and
444 Morrison, A. K.: Recent trends in the Southern Ocean eddy field, J. Geophys. Res. Oceans,
445 120, 257–267, doi:10.1002/2014JC010470, 2015.

446 Kim, Y. S., and Orsi, A. H.: On the variability of Antarctic Circumpolar Current fronts inferred
447 from 1992-2011 altimetry, J. Phys. Oceanogr., 44, 3054–3071, doi:10.1175/JPO-D-13-
448 0217.1, 2014.

449 Langlais, C., Rintoul, S. R., and Schiller, A.: Variability and mesoscale activity of the Southern
450 Ocean fronts: Identification of a circumpolar coordinate system, Ocean Modell., 39, 79–96,
451 doi:10.1016/j.ocemod.2011.04.010, 2011.

452 Moore, J. K., Abbott, M. R., and Richman, J. G.: Location and dynamics of the Antarctic Polar
453 Front from satellite sea surface temperature data, J. Geophys. Res., 104, 3059–3073,
454 doi:10.1029/1998JC900032, 1999.

455 Nowlin, W. D., and Clifford, M.: The kinematic and thermohaline zonation of the Antarctic
456 Circumpolar current at Drake Passage, J. Mar. res., 40, 481-507, 1995.

457 Orsi, A. H., Whitworth III, T., and Nowlin Jr., W. D.: On the meridional extent and fronts of the
458 Antarctic Circumpolar Current, Deep Sea Res., Part I, 42(5), 641–673, doi:10.1016/0967-
459 0637(95)00021-W, 1995.

460 Parke, M. E., Stewart, R. H. , Farless, D. L., and Cartwright, D. E.: On the choice of orbits for an
461 altimetric satellite to study ocean circulation and tides, J. Geophys. Res., 92, 11693–11707,
462 1987.

463 Pujol, M.-I., Faugere, Y., Taburet, G., Dupuy, S., Pelloquin, C., Ablain, M., Picot, N., DUACS
464 DT2014: the new multi-mission altimeter data set reprocessed over 20 years, Ocean. Sci., 12,
465 1067-1090, doi:10.5194/os-12-1067-2016, 2016.

466 Purkey, S. G., and Johnson, G. C.: Warming of global Abyssal and deep southern ocean waters
467 between the 1990s and 2000s: Contributions to global heat and sea level rise budgets, J.
468 Clim., 23, 6336–6351, doi:10.1175/2010JCLI3682.1, 2010.

469 Sallee, J. B., Speer, K., and Morrow, R.: Response of the Antarctic Circumpolar Current to
470 atmospheric variability, J. Clim., 21(12), 3020–3039, doi:10.1175/2007JCLI1702.1, 2008.

471   Shao, A. E., S. T. Gille, S. Mecking, and L. Thompson: Properties of the Subantarctic Front and
472   Polar Front from the skewness of sea level anomaly, J. Geophys. Res. Oceans, 120,
473   5179–5193, doi:10.1002/2015JC010723, 2015.
474   Sokolov, S., and Rintoul, S. R.: Multiple jets of the Antarctic Circumpolar Current south of
475   Australia, J. Phys. Oceanogr., 37, 1394–1412,doi:10.1175/JPO3111.1, 2007.
476   Sokolov, S., and Rintoul, S. R.: Circumpolar structure and distribution of the Antarctic
477   Circumpolar Current fronts: 1. Mean circumpolar paths, J. Geophys. Res., 114, C11018,
478   doi:10.1029/2008JC005108, 2009a.
479   Sokolov, S., and Rintoul, S. R.: Circumpolar structure and distribution of the Antarctic
480   Circumpolar Current fronts: 2. Variability and relationship to sea surface height, J. Geophys.
481   Res., 14, C11019, doi:10.1029/2008JC005248, 2009b.
482   Swart, N., and Fyfe, J. C.: Observed and simulated changes in the Southern Hemisphere surface
483   westerly wind-stress. Geophys. Res. Lett., 39, L16711, doi:10.1029/2012GL052810, 2012.
484   Thompson, A. F., Haynes, P. H., Wilson, C., and Richards, K. J.: Rapid Southern Ocean front
485   transitions in an eddy-resolving ocean GCM, Geophys. Res. Lett., 37, L23602,
486   doi:10.1029/2010GL045386, 2010.
487   Thompson, A. F., and Richards, K. J.: Low frequency variability of Southern Ocean jets, J.
488   Geophys. Res., 116, C09022, doi:10.1029/2010JC006749, 2011.
489   Wunsch, C.: *The Ocean Circulation Inverse Problem*, 458 pp., Cambridge Univ. Press, Cambridge, Mass.

490
491
492

Figure Captions

Figure 1. a) Mean dynamic topography in the Southern Ocean along a north-south meridian for three scenarios, and b) the corresponding geostrophic velocity, with positive values indicating eastward flow. The scenarios are: an initial state (dashed black line), a shift of the two fronts south by 60 km with no change in magnitude or shape of the currents (red line), and no shift of the mean of the current, but a change in the magnitude and shape (blue line).

Figure 2. Positions of the T/P, Jason-1, Jason-2 and Jason-3 groundtracks used for this study (black lines), and the the approximate locations of the Subantarctic Front (red line) and the Polar Front (blue line) as estimated by Orsi et al. (1995). The orange track shows the location of the pass used in analysis shown in Figures 3 and 4.

Figure 3. An example profile of mean CKE (1993-2015) along a ground track in the southern Indian Ocean (shown in orange in Figure 2), demonstrating the location of the half-power point and the locations of the southern and northern boundaries of the enhanced CKE envelope. See text for details of the computations.
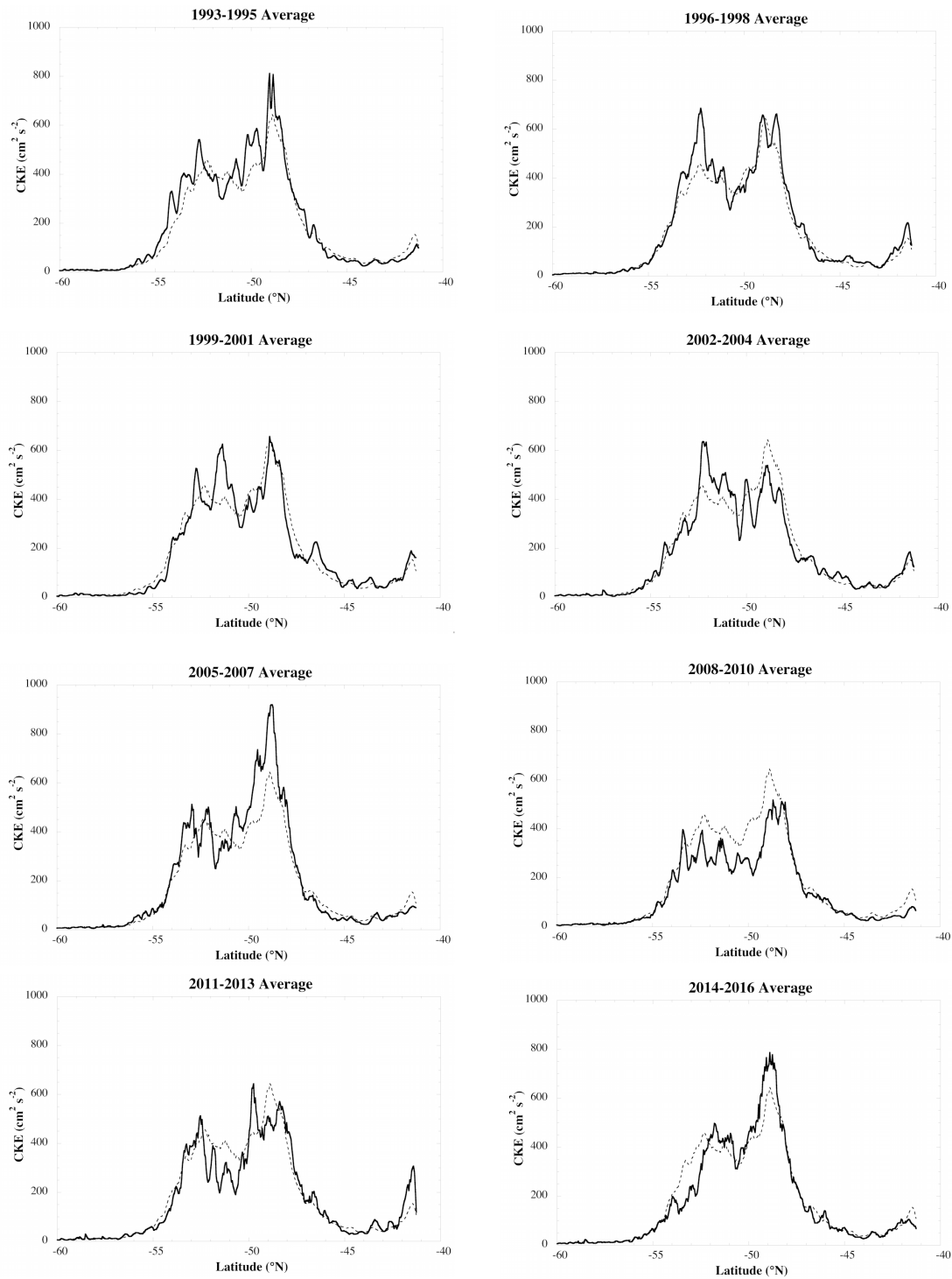
Figure 4. Three-year averages of CKE estimated along pass shown in Figure 2 (solid lines) along with the long-term mean from 1993-2016 (dotted line).
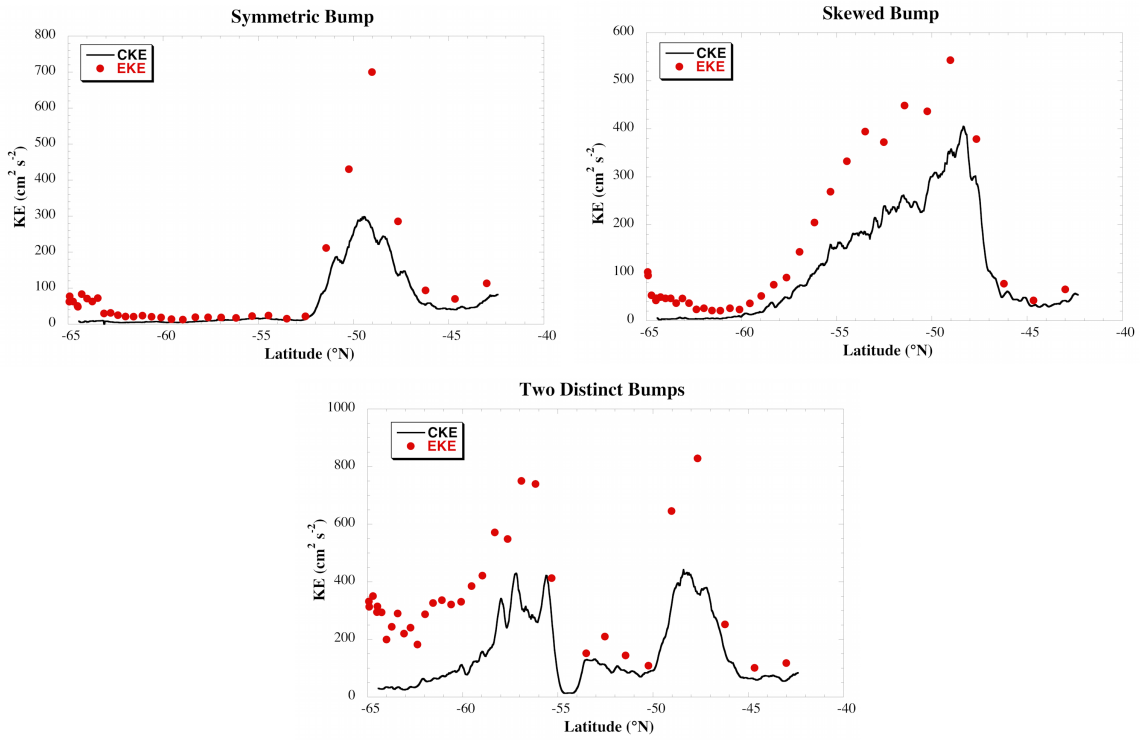
Figure 5. Examples of the three types of CKE profiles found (black lines), along with the value of the full EKE computed at crossover points.
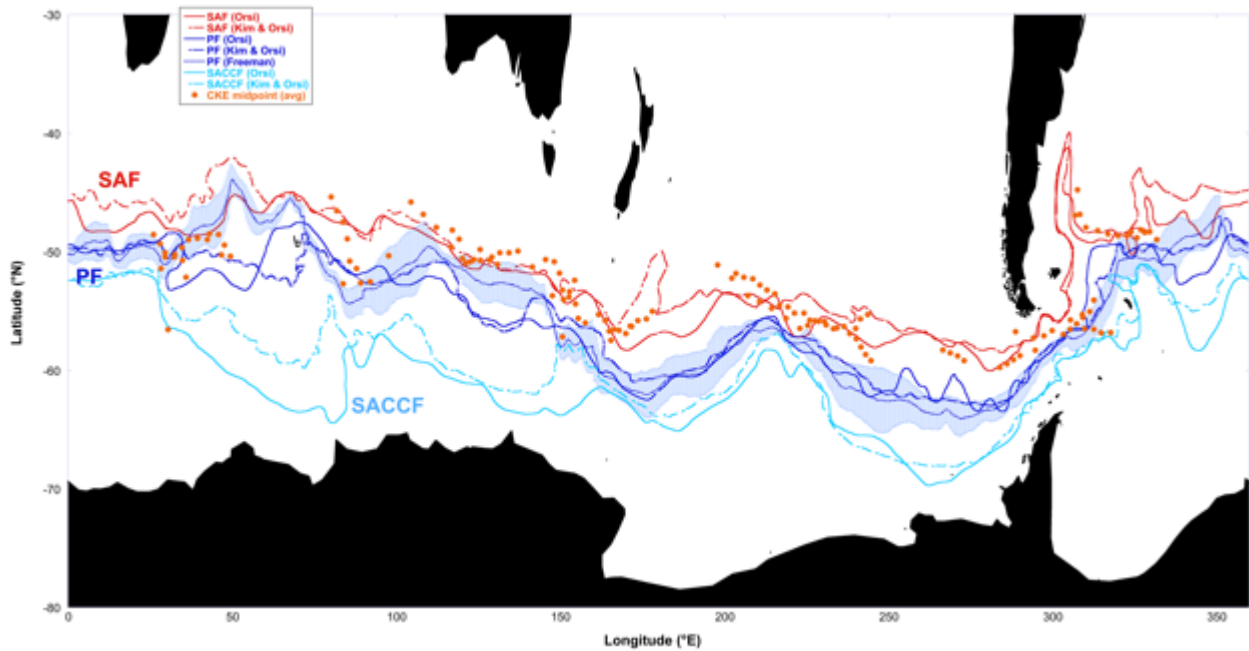
Figure 6. Mean positions of fronts estimated from CKE (orange dots) along with estimates from other authors: Orsi et al. (1995) computed using hydrographic sections, Kim and Orsi (2014) based on contours of dynamic topography, and Freeman and Lovenduski (2016a) based on gradients of sea surface temperature. The Orsi et al. (1995) fronts were downloaded from https://gcmd.nasa.gov/records/AADC_southern_ocean_fronts.html. The Freeman and Lovenduski fronts were downloaded from https://doi.pangaea.de/10.1594/PANGAEA.855640 (Freeman and Lovenduski, 2016b). The Kim and Orsi (2014) fronts were provided by Yong Sun Kim upon request.

Figure 7. Mean positions of fronts estimated from CKE (black dots) along with the percent occurrence of a jet between 1993 and 2014 computed by Chapman (2017a). Data were downloaded from http://dx.doi.org/10.5061/dryad.q9k8r (Chapman, 2017b). The percent occurrence of the jet was computed by calculating the number of times a jet occurred in the daily files, dividing by the total number of days between January 1993 and December 2014, and multiplying by 100.
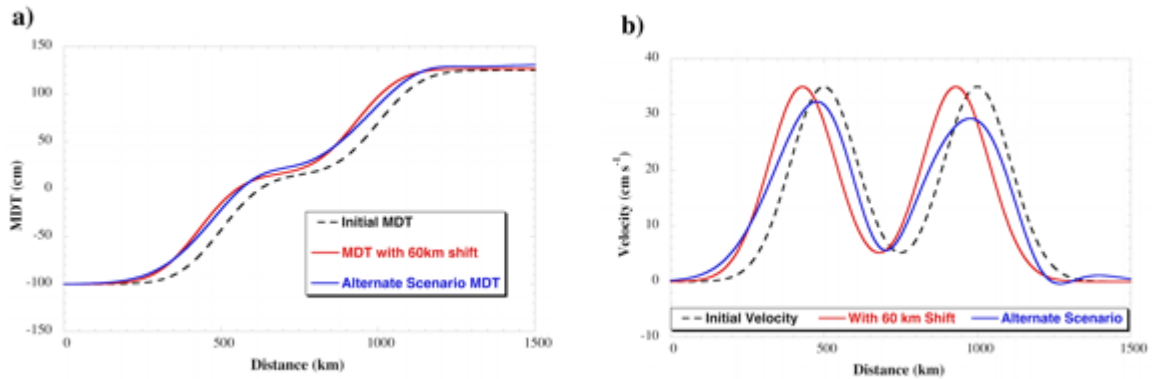
Figure 8. Estimated trend in the half-power point of CKE for each location shown in Figures 6 and 7, as a function of latitude. Error bars represent the 90% confidence interval.

Figure 9. SNR (trend/error in Figure 8). Values larger than 1 indicate a statistically significant northern shift. Values smaller than -1 indicate a statistically significant southern shift. Values between ± 1 indicate no statistically significant shift.
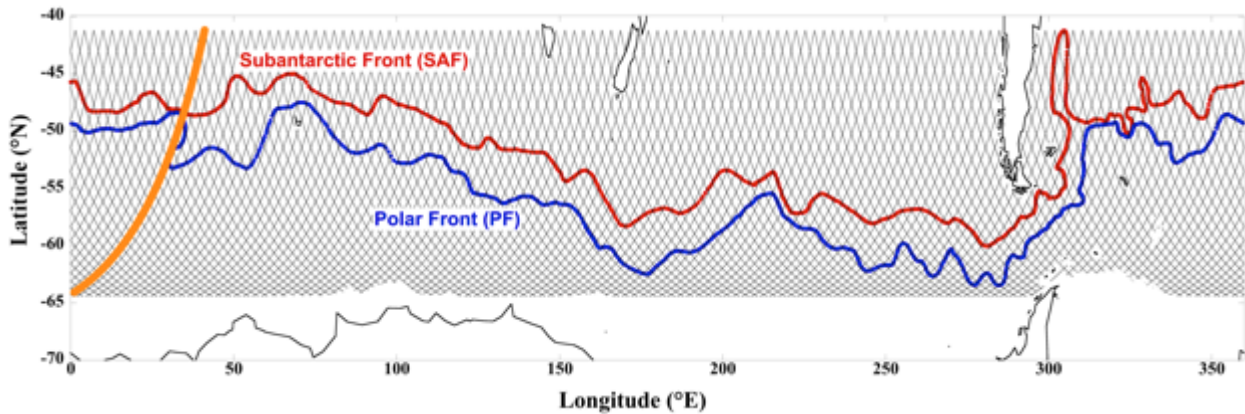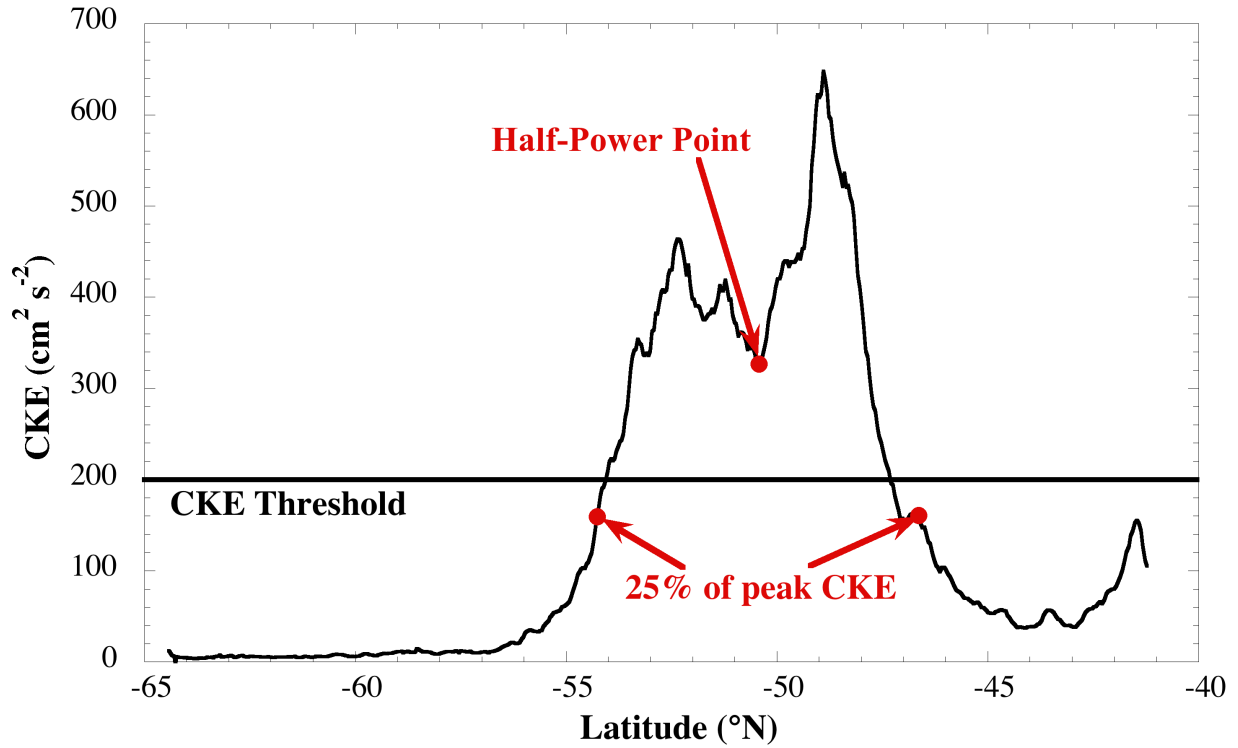
Figure 1. a) Mean dynamic topography in the Southern Ocean along a north-south meridian for three scenarios, and b) the corresponding geostrophic velocity, with positive values indicating eastward flow. The scenarios are: an initial state (dashed black line), a shift of the two fronts south by 60 km with no change in magnitude or shape of the currents (red line), and no shift of the mean of the current, but a change in the magnitude and shape (blue line).

Figure 2. Positions of the T/P, Jason-1, Jason-2 and Jason-3 groundtracks used for this study (black lines), and the the approximate locations of the Subantarctic Front (red line) and the Polar Front (blue line) as estimated by Orsi et al. (1995). The orange track shows the location of the pass used in analysis shown in Figures 3 and 4.

557
558
559 **Figure 3.** An example profile of mean CKE (1993-2015) along a ground track in the southern
560 Indian Ocean (shown in orange in Figure 2), demonstrating the location of the half-power point
561 and the locations of the southern and northern boundaries of the enhanced CKE envelope. See
562 text for details of the computations.
563
564

565

566
Figure 4. Three-year averages of CKE estimated along pass shown in Figure 2 (solid lines)
along with the long-term mean from 1993-2016 (dotted line).

569

570

571

572

573 **Figure 5.** Examples of the three types of CKE profiles found (black lines), along with the value
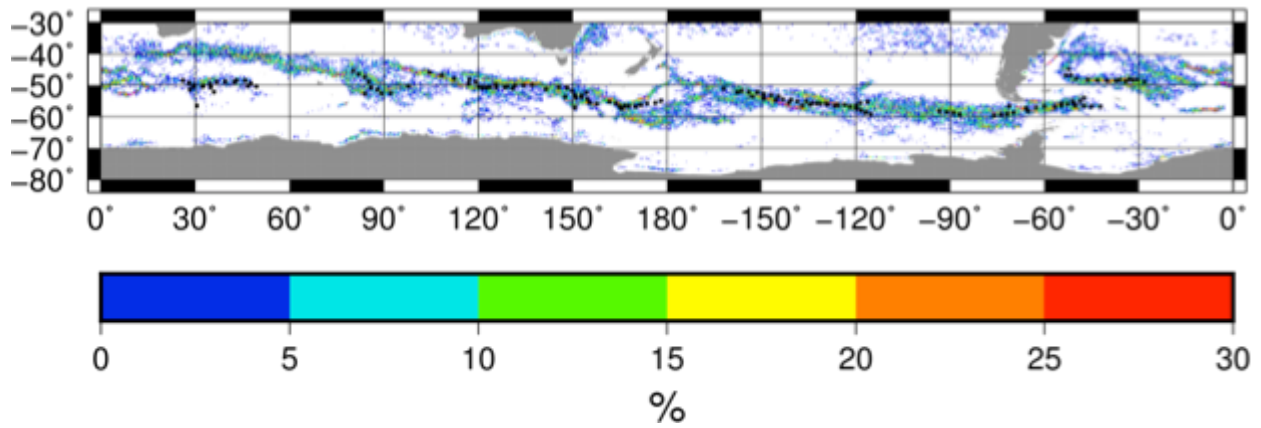574 of the full EKE computed at crossover points.

575

576

577

578
579

580
581
582 **Figure 6.** Mean positions of fronts estimated from CKE (orange dots) along with estimates from
583 other authors: Orsi et al. (1995) computed using hydrographic sections, Kim and Orsi (2014)
584 based on contours of dynamic topography, and Freeman and Lovenduski (2016a) based on
585 gradients of sea surface temperature. The Orsi et al. (1995) fronts were downloaded from
586 https://gcmd.nasa.gov/records/AADC_southern_ocean_fronts.html. The Freeman and
587 Lovenduski fronts were downloaded from https://doi.pangaea.de/10.1594/PANGAEA.855640
588 (Freeman and Lovenduski, 2016b). The Kim and Orsi (2014) fronts were provided by Yong Sun
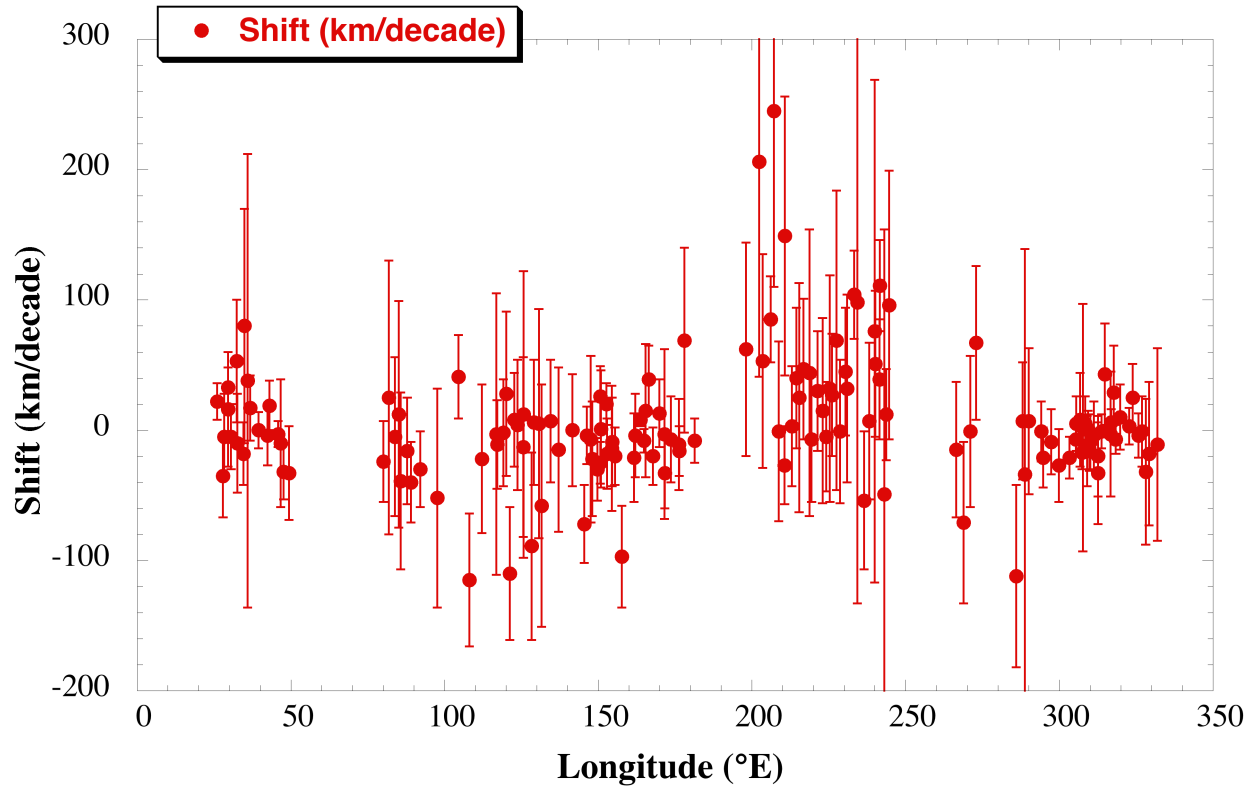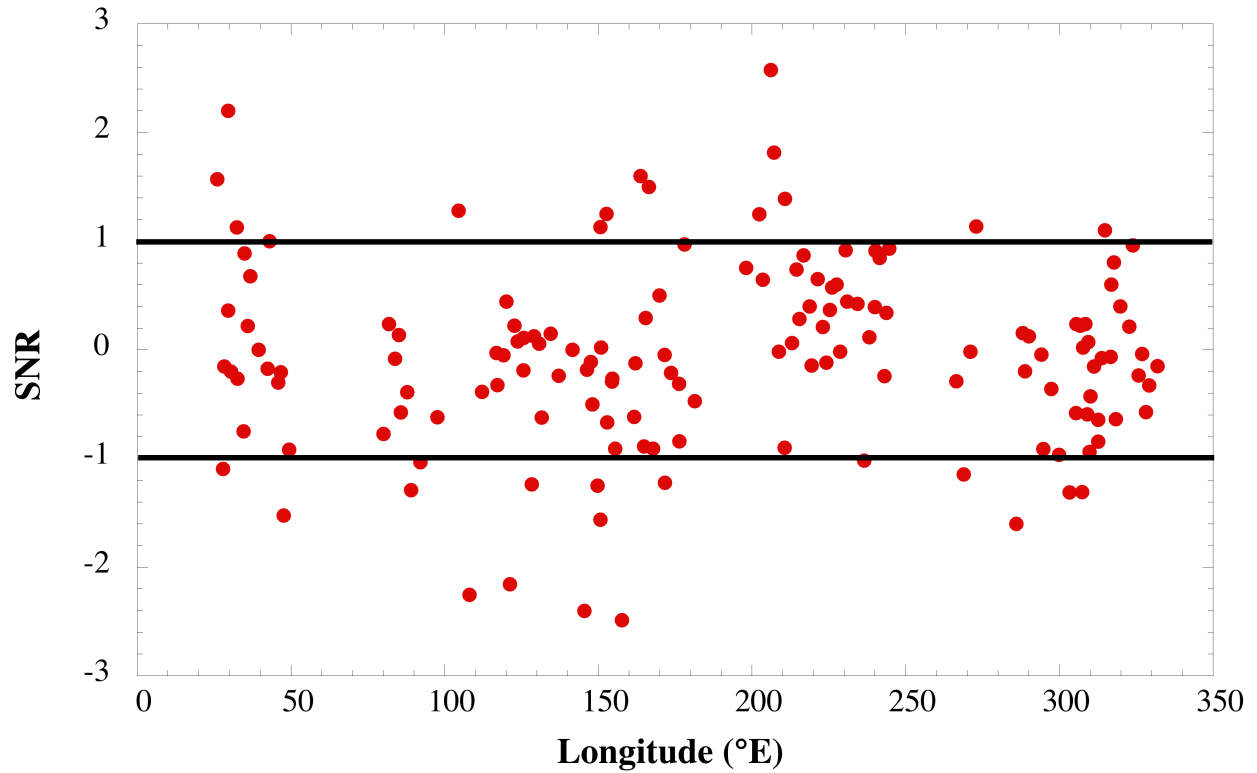589 Kim upon request.
590

591

592
593
594 **Figure 7.** Mean positions of fronts estimated from CKE (black dots) along with the percent
595 occurrence of a jet between 1993 and 2014 computed by Chapman (2017a). Data were
596 downloaded from http://dx.doi.org/10.5061/dryad.q9k8r (Chapman, 2017b). The percent
597 occurrence of the jet was computed by calculating the number of times a jet occurred in the daily
598 files, dividing by the total number of days between January 1993 and December 2014, and
599 multiplying by 100.
600

Figure 8. Estimated trend in the half-power point of CKE for each location shown in Figures 6 and 7, as a function of latitude. Error bars represent the 90% confidence interval.

607
608
609 **Figure 9.** SNR (trend/error in Figure 8). Values larger than 1 indicate a statistically significant
610 northern shift. Values smaller than -1 indicate a statistically significant southern shift. Values
611 between ± 1 indicate no statistically significant shift.
612
613